Novel magnetic stoichiometric superconductor compound EuRbFe₄As₄

T K Kim, K S Pervakov, V A Vlasenko, A V Sadakov, A S Usol'tsev, D V Evtushinsky,
S Jung, G Poelchen, K Kummer, D Roditchev, V S Stolyarov, I A Golovchanskiy,
D V Vyalikh, V Borisov, R Valentí, A Ernst, S V Eremeev, E V Chulkov, V M Pudalov

Contents

Abstract. In the new stoichiometric high-temperature iron-based superconductor RbEuFe₄As₄, superconductivity coexists with a peculiar long-range magnetic order of the Eu 4f states; their coexistence is an enigma and a challenge for both experiment and theory. Using angle-resolved photoemission spectroscopy (ARPES), resonant photoemission spectroscopy (ResPES), Andreev reflection spectroscopy, scanning tunneling spectroscopy, and DFT band structure calculations, we have made significant progress in solving this puzzle. Our results unambiguously indicate a separation between the electronic states of Fe (superconductivity) and Eu (magnetism) and demonstrate the existence of superconducting and long-range magnetic orders almost independently of each other.

1. Introduction

Superconducting compounds, including atoms with a large spin magnetic moment (Gd^{3+}, Eu^{2+}, etc.), are remarkable objects for studying such fundamental problems of condensed matter physics as the interplay of magnetic ordering and superconducting pairing [1]. Magnetism has traditionally been viewed as a phenomenon antagonistic towards superconductivity; nevertheless, as is now well known, there are many classes of materials with unconventional superconduc-

T K Kim [(1)], **K S Pervakov** [(2)], **V A Vlasenko** [(2)], **A V Sadakov** [(2)],
A S Usol'tsev [(2)], **D V Evtushinsky** [(3)], **S Jung** [(1)], **G Poelchen** [(4, 5)],
K Kummer [(5)], **D Roditchev** [(6, 7, 8)], **V S Stolyarov** [(8, 9, 10)],
I A Golovchanskiy [(8, 9, 10)], **D V Vyalikh** [(11, 12)], **V Borisov** [(13)], **R Valentí** [(13)],
A Ernst [(14, 15)], **S V Eremeev** [(16)], **E V Chulkov** [(11, 17, 18)], **V M Pudalov** [(2, 19, *)]

(1) Diamond Light Source, Harwell Campus, OX11 0DE Didcot,
    United Kingdom
(2) Lebedev Physical Institute, Russian Academy of Sciences,
    Leninskii prosp. 53, 119991 Moscow, Russian Federation
(3) Laboratory for Quantum Magnetism, Institute of Physics,
    École Polytechnique Fédérale de Lausanne,
    CH-1015 Lausanne, Switzerland
(4) Institut für Festkörper- und Materialphysik,
    Technische Universität Dresden, D-01062 Dresden, Germany
(5) European Synchrotron Radiation Facility, Grenoble, France
(6) LPEM, ESPCI Paris, PSL Research University,
    CNRS, 75005 Paris, France
(7) Sorbonne Université, CNRS, LPEM, 75005 Paris, France
(8) Moscow Institute of Physics and Technology
    (National Research University), Institutskii per. 9,
    141701 Dolgoprudny, Moscow region, Russian Federation
(9) Dukhov Research Institute of Automatics,
    ul. Sushchevskaya 22, 119017 Moscow, Russian Federation
(10) National University of Science and Technology MISIS,
    Leninskii prosp. 4, 119049 Moscow, Russian Federation

(11) Donostia International Physics Center,
    20018 Donostia-San Sebastián, Basque Country, Spain
(12) IKERBASQUE, Basque Foundation for Science, 48013 Bilbao, Spain
(13) Institut für Theoretische Physik, Goethe-Universität Frankfurt,
    D-60438 Frankfurt am Main, Germany
(14) Institut für Theoretische Physik, Johannes Kepler Universität,
    A 4040 Linz, Austria
(15) Max-Planck-Institut für Mikrostrukturphysik,
    D-06120 Halle, Germany
(16) Institute of Strength Physics and Materials Science,
    Siberian Branch of the Russian Academy of Sciences,
    Akademicheskii prosp. 2/1, 634055 Tomsk, Russian Federation
(17) St. Petersburg State University, Universitetskaya naberezhnaya 7-9,
    199034 St. Petersburg, Russian Federation
(18) Departamento de Fízica de Materiales UPV/EHU and Centro de
    Fízica de Materiales (CFM-MPC), Centro Mixto CSIC-UPV/EHU,
    20080, Donostia-San Sebastián, Basque Country, Spain
(19) National Research University Higher School of Economics,
    ul. Myasnitskaya 20, 101000 Moscow, Russian Federation
E-mail: (*) pudalov@lebedev.ru

tivity, from heavy fermion compounds and borocarbides to copper oxides, in which the superconducting state is closely related to or even arises from magnetism.

Among recently intensively studied iron pnictides, the EuFe$_2$As$_2$ compound [2, 3] ignited great interest in the fact that, besides the antiferromagnetic (AFM) ordering of Fe electrons in a spin-density-wave type structure (at high temperatures $\sim$ 195 K), at lower temperatures of $\sim$ 19 K, in the superconducting region, a long-range magnetic order sets in the Eu^{2+}. In the low-temperature magnetic state, the spins of the electrons of Eu are ordered ferromagnetically in the *ab* plane and antiferromagnetically along the *c*-axis [4]. As a result, the original parent compound EuFe$_2$As$_2$ is an insulator, but when doped or when the lattice is deformed under pressure, it becomes a superconductor.

Thus, in doped EuFe$_2$(As$_{1-x}$P$_x$)$_2$, for $x \sim 0.2$, superconductivity below $T_m \approx 19$ K coexists with magnetically-ordered subsystem of Eu electrons [5–14]. Such a coexistence does not lead to deviations of the superconducting state from the conventional one with the singlet type pairing [5, 6]. This contrasts with the known behavior in borocarbides, for which lattice doping with rare-earth magnetic ions leads to a decrease in the critical temperature [15]. The apparent complete independence of the superconducting properties of electrons from the magnetic ordering of the Eu sublattice is associated with the multiorbital nature of iron-based superconductors, in which the exchange interaction and superconductivity are provided by different groups of electrons.

In 2016, a new family of superconducting iron pnictides was discovered, so-called 1144-type compounds AeAFe$_4$As$_4$, (where Ae = Ca, Sr, La, Eu and A = K, Rb, Cs) [16]. These compounds demonstrate more intriguing properties than Eu-122 due to the fact that they are superconductors in stoichiometric composition. As in 122-compounds, atoms with a large spin magnetic moment (Gd^{3+}, Eu^{2+} and others) built into the crystal lattice tend to magnetic ordering.

The Meissner state in magnetic superconductors of the 1144 family turns out to be nontrivial: it coexists with short-scale ferromagnetic domains with dimensions smaller than the field penetration depth and at low temperatures transforms into a very interesting domain-vortex state [8, 9]. Small sizes of magnetic domains are necessary for the existence of a superconducting state at temperatures below T_m [17]. In this state, a self-generated entrance of vortices at temperatures near T_m was discovered in Ref. [18]. The increase in magnetic induction B observed in [18] is most pronounced at T_m. This unusual behavior of B, as opposed to the usual pushing out of the magnetic field in conventional superconductors, is a consequence of the collective reaction of the magnetic and superconducting subsystems in EuRbFe$_4$As$_4$.

The unusual properties of the magnetic superconducting compound motivated us to carry out comprehensive studies of the thermodynamic magnetic properties and the amplitude of the superconducting order parameter, as well as the band structure, particularly in the vicinity of the Fermi level for carriers responsible for superconductivity, and the structure of the electronic states of Eu and its spin state.

2. Experiment

2.1 Crystal lattice

AeAFe$_4$As$_4$ compounds have the tetragonal crystal lattice ($P4/mmm$), in which the Ae and A layers form two non-

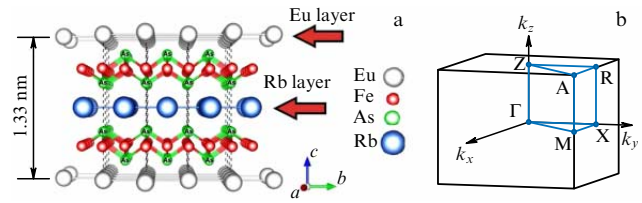**Figure 1.** (Color online.) (a) Crystal structure of EuRbFe$_4$As$_4$. Red arrows show the cleavage planes (taken from [19]). (b) Bulk Brillouin zone of EuRbFe$_4$As$_4$.

equivalent structures [16]. In particular, in EuRbFe$_4$As$_4$ (Fig. 1), in contrast to the '122' parent compound, EuFe$_2$As$_2$ and RbFe$_2$As$_2$ blocks alternate along the *c*-axis [16, 20–23]. As a result of the different ionic radii Eu and Rb atoms have, such a two-block structure turns out to be strained. This factor, as well as the redistribution between Eu- and Rb- layers of a small number (5–10%) of atoms, leads to self-doping of the nominally stoichiometric compounds with *p*-type carriers (0.25 holes per Fe atom); as a result, a superconducting state emerges with a critical temperature $T_c \approx 36$ K. Magnetic ordering in the Eu sublattice occurs at temperature $T_m \sim 15$ K, inside the domain of the superconducting state. Due to the missing mirror symmetry along the *c*-axis, in EuRbFe$_4$As$_4$ (in contrast to EuFe$_2$As$_2$), the magnetic order emerging below the Curie temperature is a helicoidal antiferromagnet structure [14, 24, 25].

2.2 Samples

High-quality single crystals of EuRbFe$_4$As$_4$ were grown by the self-flux technique. The initial high purity components of Eu (99.95%), Rb (99.99%), and the pre-synthesized precursor FeAs (99.98% Fe + 99.9999% As) were mixed at a 1:1:12 molar ratio. The mixture was placed into an alumina crucible and welded vacuum-tight into an Nb container under a 0.2 atm residual pressure of argon. The container was then placed in a tube oven with an argon atmosphere and the furnace was heated to 1250 °C, kept at this temperature for 24 h for homogenization of the melt, and then cooled to 900 °C at a rate of 2 °C h^{-1}. At this temperature, the container with the crystal was kept for another 24 hours to reduce the concentration of growth defects and then finally cooled to room temperature inside the furnace. The large-size crystals were removed from the crucible in an Ar atmosphere in an Ar glove box. Finally, the crystals were transported to the measuring devices in a sealed container, with minimal time exposure to air. The appearance of representative crystals are shown in the inset in Fig. 2. They had typical dimensions up to 3 mm in the basal plane with large areas of an atomically-flat surface (see Fig. 2).

The X-ray diffraction pattern of the obtained crystals, shown in Fig. 3, indicates the presence, in addition to the dominant phase of Eu-1144, of a small amount of the impurity Eu-122 phase, which inevitably arises in the process of synthesis. Elemental analysis in the mapping mode (Table 1) at 9 different regions points out a uniform distribution of the elements over the sample surface (see inset in Fig. 2). We found that the factual chemical composition of our single crystal was Eu$_{1.06(2)}$Rb$_{0.81(2)}$Fe$_{3.92(5)}$As$_{4.00(5)}$. The minor excess of Eu atoms is due to the presence of about 10% EuFe$_2$As$_2$ phase; the TEM results reveal that this side phase is present as short
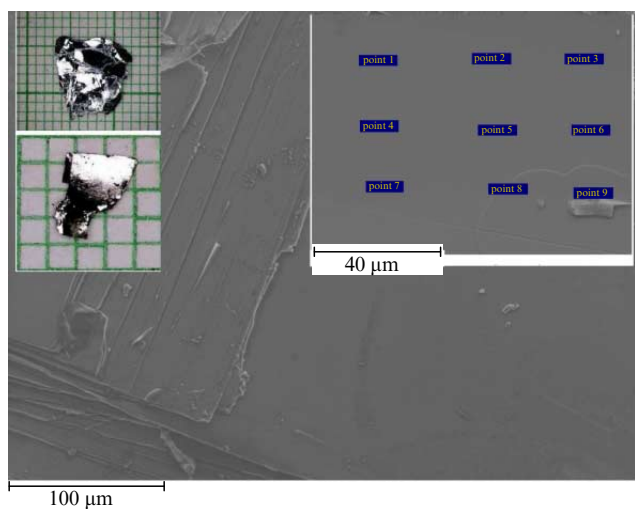
Figure 2. SEM (Scanning Electron Microscope) image of a crystal cleavage surface. Left inset: optical image; right: enlarged image of a flat area of the surface showing regions of the EDX measurement of elemental composition.
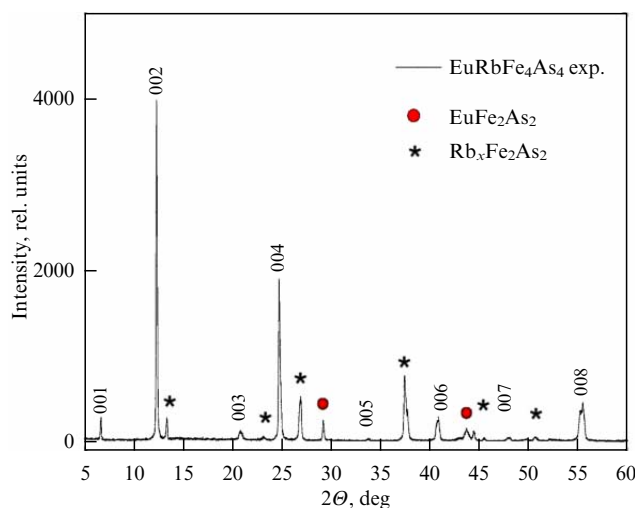

Figure 3. (Color online.) X-ray diffraction pattern of the $EuRbFe_4As_4$ single crystal. Asterisks mark the peaks corresponding to the Eu-122 side phase. (Adapted from [26].)

Table 1. Elemental composition of $EuRbFe_4As_4$ crystals (in weight %) in 9 surface regions, shown in Fig. 2.

Region	Fe	As	Rb	Eu	Total
1	28.26	37.98	9.11	24.65	100.00
2	28.37	38.18	8.79	24.66	100.00
3	28.16	38.09	8.83	24.91	100.00
4	27.96	38.39	8.81	24.85	100.00
5	27.91	38.49	8.82	24.78	100.00
6	27.86	38.35	8.68	25.10	100.00
7	27.92	38.39	8.69	25.00	100.00
8	27.81	38.55	8.73	24.92	100.00
9	28.18	39.05	9.34	23.43	100.00
Average	28.05	38.39	8.87	24.70	100.00
σ	0.20	0.31	0.22	0.50	

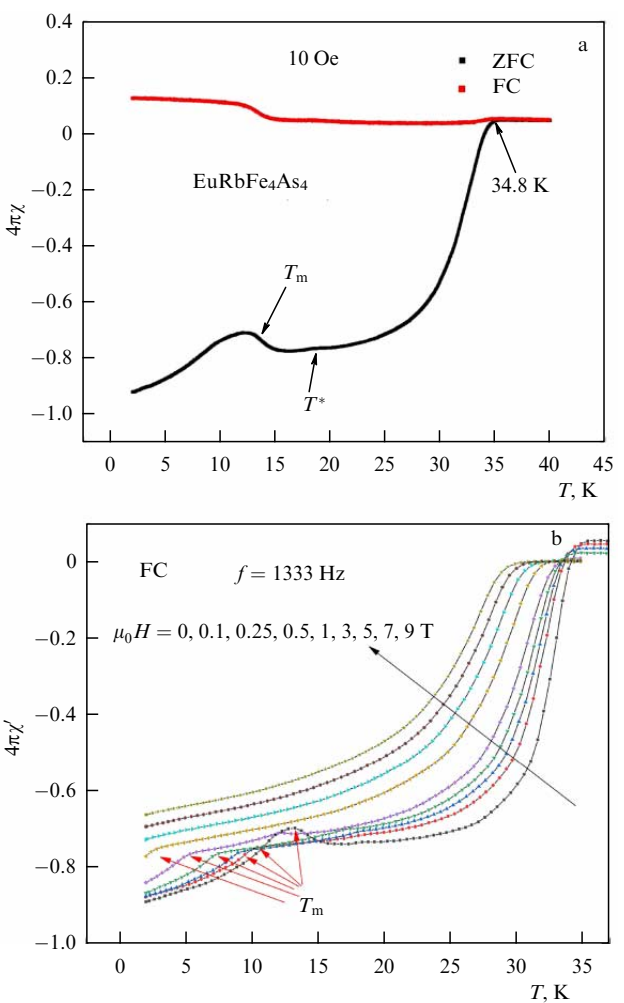irregular atomic chains between the planes of the majority Eu-1144 phase.

Figure 4. (Color online.) (a) Temperature dependence of DC magnetic susceptibility for cooling in a zero field (ZFC) and in an external field (FC) of 10 Oe applied in the *ab* plane. (b) Temperature dependence of the real part of the magnetic susceptibility at various field values. (Adapted from [26].)

2.3 Magnetic and superconducting properties from thermodynamic measurements

The temperature dependence of the DC magnetic susceptibility χ (Fig. 4) shows a sharp diamagnetic transition upon cooling in a zero field (ZFC mode) at $T_c \approx 35$ K due to a superconducting transition; the volume fraction of the superconducting phase is $\sim 90\%$ at 2 K.

In the superconducting state, at $T \approx 12 - 16$ K, the DC susceptibility has a peak indicating the onset of magnetic ordering in the sublattice of Eu atoms. The temperature dependence of the AC susceptibility (see Fig. 4) also shows a peak at the same temperature $T_m \approx 15$ K. In a magnetic field H applied in the *ab* plane, as the field increases, the peak shifts towards lower temperatures and completely disappears at $H \approx 3$ T, which allows us to estimate roughly the exchange field as ~ 3 T in the plane of Eu atoms. The lowest arrow in Fig. 4a marks temperature $T^* = 19$ K that is the known point of AFM ordering in the Eu-122 compound [5]; the absence of features in $\chi(T)$ at 19 K confirms that the amount of this side phase in the studied crystals is negligibly small.

The $M(H)$ curves (Fig. 5) also demonstrate the superposition of the diamagnetic superconducting hysteresis at
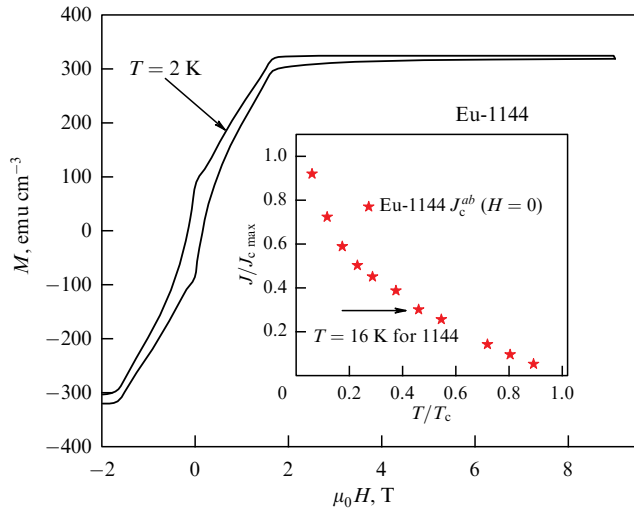
Figure 5. (Color online.) Magnetization curve at $T = 2$ K. Inset shows temperature dependence of critical current J_c^{ab} normalized to its maximum value. (Adapted from [26].)

$T < T_c$ associated with vortex pinning and (at $T < T_m$) magnetization curves with a saturation in a field 2 T typical of ferromagnetic ordering [26]. Magnetization $M(H)$ measurements were carried out with field orientation in the *ab* plane, at a field sweep rate of 100 Oe s^{-1}. From the magnetization saturation field in Fig. 5 of ≈ 310 emu cm^{-3} at $T = 2$ K, we obtain an estimate for the magnetic moment of the Eu atoms of $6.4\mu_B$ (μ_B is the Bohr magneton), which is in good agreement with the tabular value of $7\mu_B$.

The M versus H hysteresis in Fig. 5 barely changes when passing through the temperature T_m; therefore, we conclude that it is associated only with vortices pinning in the superconducting state. This enables us to estimate the critical current J_c from the width of the hysteresis loop $\Delta M(H)$ using Bean models [27]. The normalized J_c values as a function of the normalized temperature are shown in the inset in Fig. 5. These $M(H)$ curves have a form typical of the superconducting compounds of the 'Ba-122' and 'CaK-1144' families, which do not contain magnetic atoms [26]. We conclude that the susceptibility, high field magnetization, and critical current are not sensitive to the presence of strong magnetism of Eu atoms.

2.4 Superconducting properties from Andreev reflection spectroscopy, ARPES, and STS

Andreev reflection spectroscopy was measured using the break-junction (BJ) technique [28–33]. For measurements, the sample shaped like a flat plate (in the *ab* plane) was attached to an isolated springy sample stage made of Be-bronze. The sample was fixed with a conductive paste at 4 points to enable 4-contact measurements of the current–voltage $(I\!-\!V)$ characteristics and dynamic conductance $(dI/dV$ *vs* $V)$. To create microcracks in the bulk of the crystal, the stage with the sample was precisely deformed in a liquid helium environment at 4.2 K, which prevented the microcracks from becoming contaminated and oxidized. To form the S$-$N$-$S junction (or, more precisely, the 'super-conductor–constriction–superconductor'), the microcrack edges of the crystal were precisely tuned (by mechanically bending the stage), until the desired Andreev reflection regime was achieved. In this regime, the current–voltage character-

istic exhibits a pronounced excess current (increase in conductivity) in the vicinity of zero voltage offset [34].

In the Andreev reflection mode, within the superconducting (SC) temperature range $T < T_c$, in the dynamic conductivity $(dI/dV$ *vs* $V)$ of the S$-$N$-$S contact minima appear at discrete values of the bias voltage [29, 34, 35]. These minima are associated with first-order resonances at $V = 2\Delta_i/e$, where Δ_i is the gap value for the ith SC condensate, and e is the elementary charge. When the sample is split in BJ experiments, in addition to a single S$-$N$-$S junction, chains of series-connected S$-$N$-$S junctions often form. For such chains, the resonant features of Andreev reflection are observed at bias voltages $V_m = m(2\Delta_i/e)$ (where $m = 2, 3, \ldots$); the resulting spectrum may be easily found by scaling the bias voltage with respect to integer values of m [29, 30].

Within the current–voltage characteristic (Fig. 6a), the enhanced conductivity is seen in the range of ± 10 mV, typical of the Andreev reflection regime. On the dynamic conductivity dI/dV curves (Fig. 6a), one can see minima at bias voltages $V = \pm 8.6$ and ± 14.5 mV, indicating the presence of two superconducting condensates with a 'large' Δ_L and a 'small' Δ_S superconducting gap, respectively. As the temperature rises, the positions of the minima shift towards lower voltages and converge to zero at the same value $T_c \approx 35$ K. This value is consistent with the bulk T_c determined from simultaneous measurements of conductivity, as well as from thermodynamic measurements of susceptibility and magnetization carried out on samples from the same batch.

The general evolution of the gap amplitudes with temperature is shown in Fig. 6b. It clearly shows the presence of at least two gaps in the spectrum, Δ_L and Δ_S. The positions of the two major minima in dI/dV as a function of temperature are given in Fig. 6c. By extrapolating the $\Delta_i(T)$ values to $T = 0$, using the BCS (Bardeen–Cooper–Schrieffer) type dependence, we obtain $\Delta_L(0) = 7.25 \pm 0.3$ meV and $\Delta_S(0) = 4.3 \pm 0.2$ meV. With these gap values, the characteristic ratios are $2\Delta_L/(k_B T_c) = 4.80$ and $2\Delta_S/(k_B T_c) = 2.85$, where k_B is the Boltzman constant.

From the data in Fig. 6c, one can draw an important conclusion: both dependences, $\Delta_{L,S}(T)$, develop gradually with no features through the temperature $T_m \approx 15$ K of Eu magnetic ordering. The absence of features in $\Delta_i(T)$ in the vicinity of magnetic ordering T_m, as well as the gap values, agrees with the ARPES (Angle-Resolved PhotoEmission Spectroscopy) data, where the gap values were linked with the well defined Fermi surface (FS) sheets in the momentum space [36]. Thus, both Andreev reflection spectroscopy and ARPES clearly indicate that the amplitude of the superconducting order parameter in RbEuFe$_4$As$_4$ is insensitive to the magnetic ordering of the sublattice of Eu atoms.

From high resolution ARPES measurements in Ref. [36], the opening of a superconducting gap was observed in the electron and hole regions of the FS at temperatures below T_c. Since ARPES measurements are momentum resolved, the gap values Δ_i may be tied to the FS pockets: the largest gap opens on the FS inner hole cylinder, as well as in other iron-pnictides of the 122 family [37–39]. Within the measurement uncertainty, the same value of ≈ 9 meV has a gap at the electron pocket. In general, the gap values Δ_i determined from ARPES are in agreement with those determined from BJ measurements. We stress that there are no singularities at temperatures near T_m on the temperature dependence of the gap obtained from
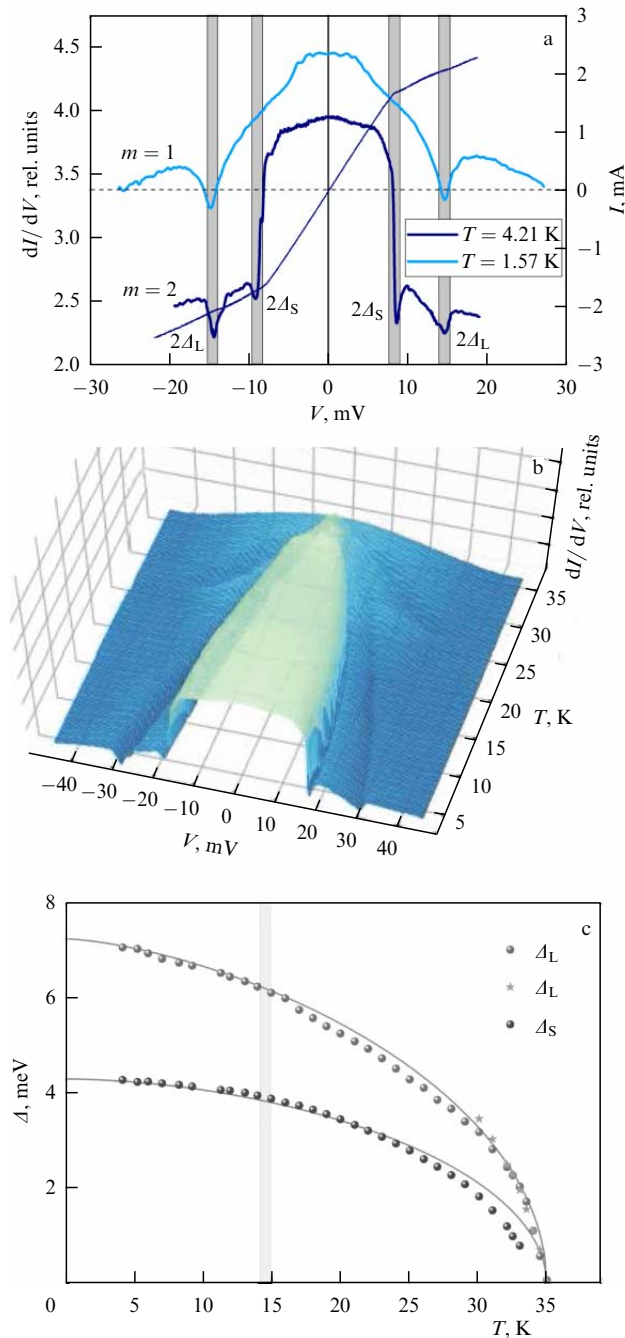
Figure 6. (Color online.) (a) Typical $I-V$ characteristics (right Y-axis), and dynamic conductivity (left Y-axis) for two different junctions: single and double-stack. In the latter case, the voltage is scaled down by $m = 2$ times. Shaded vertical stripes highlight positions of dI/dV minima. (b) 3D picture of a complete set of dI/dV curves versus bias voltage V and T for double-stack junction $m = 2$. V_i values are doubled here as compared with panel a. (c) Temperature dependence of two strongest gap features obtained from dI/dV minima. Green circles represent the large gap, blue ones, the small gap. Red asterisks illustrate the reproducibility of the data in various measurements. Solid gray lines represent a BCS-like fit. Panels a and c are adapted from [36].

ARPES [36] nor on the dependence from BJ measurements (see Fig. 6c).

Local measurements using scanning tunneling spectroscopy (STS) also revealed a superconducting gap [19]; however, quantitative measurements of it were impeded by the fact that the cleaved crystal surface of EuRb-1144

corresponds to the 'nonsuperconducting planes' of Eu and Rb atoms located far from FeAs 'superconducting planes'.

2.5 Band structure, Fermi surface, and Eu energy levels from ARPES and STS measurements, and from calculations

Figure 7a shows a Fermi surface map in the $k_x - k_y$ plane (for $k_z = 0$, i.e., around the Γ point) measured at a photon energy of 70 eV. It can be seen that the FS for EuRb-1144 is qualitatively similar to that of optimally doped $Ba_{1-x}K_xFe_2As_2$ (so-called 'Ba-122') ferropnictides [37, 38] and consists of three nested hole cylinders in the center of the Brillouin zone and more complex electronic pockets in the corners of the Brillouin zone.

The band dispersion measured in the $M-\Gamma-M$ direction (Fig. 7b) includes, besides the branches originating mainly from 3d Fe orbitals, branches from Eu 4f orbitals, ranging from 1.0 to 1.7 eV below the Fermi level. This ARPES result is consistent with the band structure calculations given in Fig. 7d, where a bunch of almost flat Eu-zones is seen in the region around -1.7 eV. Thus, the spectral density of Eu 4f states lies far away in energy from the electronic states of Fe near the Fermi level, which are the states involved in superconducting pairing. For this reason, one cannot expect a noticeable contribution of the Eu states to superconducting pairing either. The measured Fermi surface cross sections and the band structure are in good agreement with the results of density functional theory (DFT) calculations (see Fig. 7d and also Ref. [36]).

The results described above of ARPES measurements of energy levels for Eu atoms are confirmed by measurements of the tunneling conductivity. A typical tunneling conductivity spectrum measured by STS is shown in Fig. 7c. In this figure, a resonance is visible at bias voltage $V_T \approx -1.8$ V. The position of this resonance is consistent with the ARPES results (Fig. 7b) and DFT calculations (Fig. 7d).

2.6 Eu magnetic levels from ResPES measurements and calculated magnetic structure of the Eu sublattice

The fine structure of Eu levels was measured in Ref. [36] by resonant photoemission spectroscopy (ResPES) at the absorption threshold of Eu $4d \rightarrow 4f$ using photons with an energy of 142 eV. The measurements were carried out by systematically varying the temperature from 40 to 5 K, i.e., in the normal state, via the superconducting state with a magnetically disordered Eu sublattice ($35 > T > 15$ K) into the magnetically ordered superconducting state ($T < 15$ K); the results are shown in Fig. 8. The divalent Eu state with a $4f^7$ electron configuration has a large and purely spin magnetic moment $7\mu_B$, which determines the complex magnetic properties of the Eu sublattice.

As can be seen from Fig. 8, when the temperature drops well below $T_m \approx 15$ K, the spectral weight is transferred from the side resonances to the central peak corresponding to the ground state. This can be explained as the appearance of the long-range FM order of the 4f moments in the Eu layer. When the FM order sets in due to exchange interaction, which couples neighboring 4f moments, the angular momenta assume a long-range orientation leading to a preferred direction between incoming light and angular momentum, implying a different excitation probability for the ferromagnetically ordered 4f states than for the paramagnetically disordered 4f states with a nearly isotropic angular momentum orientation. The inset in this figure shows a wide 'tail' of
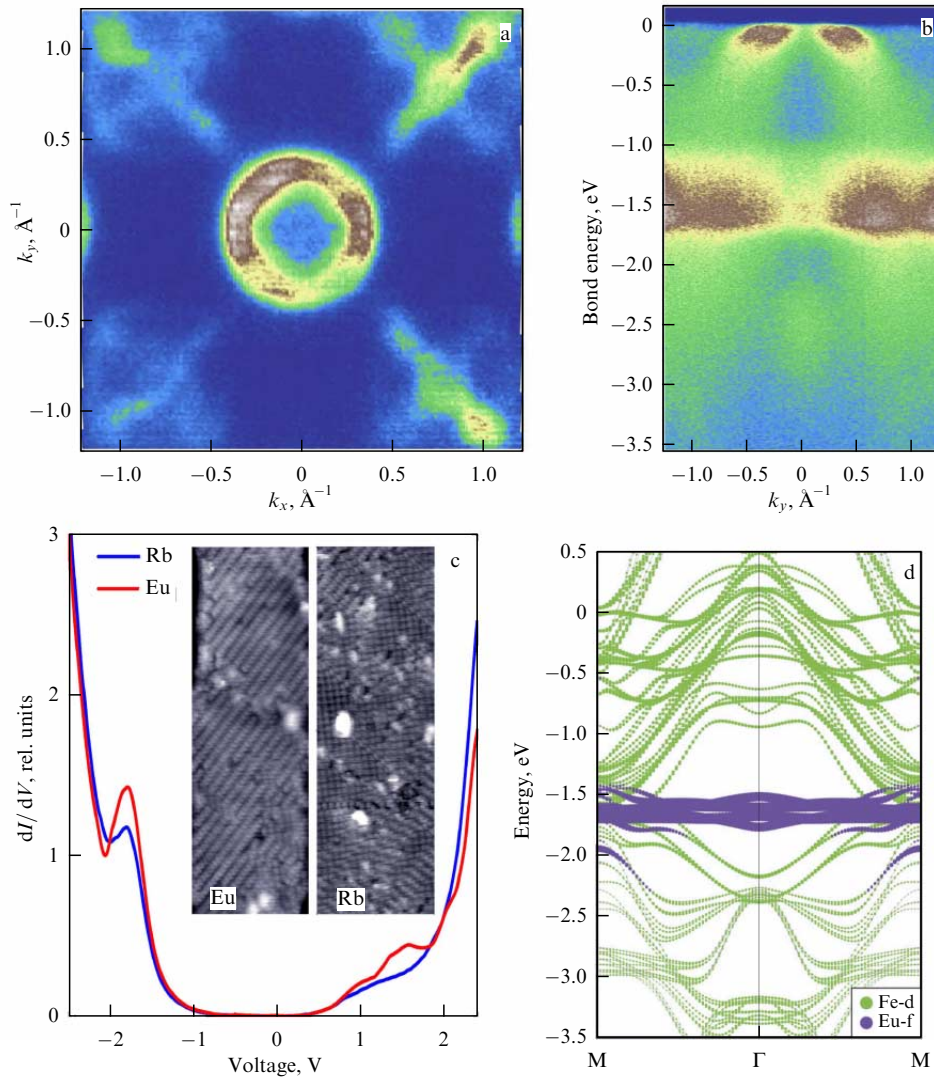
Figure 7. (Color online.) (a) Map of the FS cross section by the $k_z = 0$ plane, measured at $T = 40$ K with a photon energy of 70 eV. (b) Dispersion in the M$-\Gamma-$M direction measured with a photon energy of 113 eV. Brown corresponds to the photoemission intensity maximum, dark blue, to the intensity minimum. (c) Tunneling conductivity dI/dV versus V determined two different terminations, Eu and Rb, respectively. Insets show 14×40 nm^2 areas, where averaged spectra were obtained. (d) Calculated band dispersion in M$-\Gamma-$M direction: Fe-3d bands shown with green lines, Eu-4f bands, with violet. (Adapted from [36].)
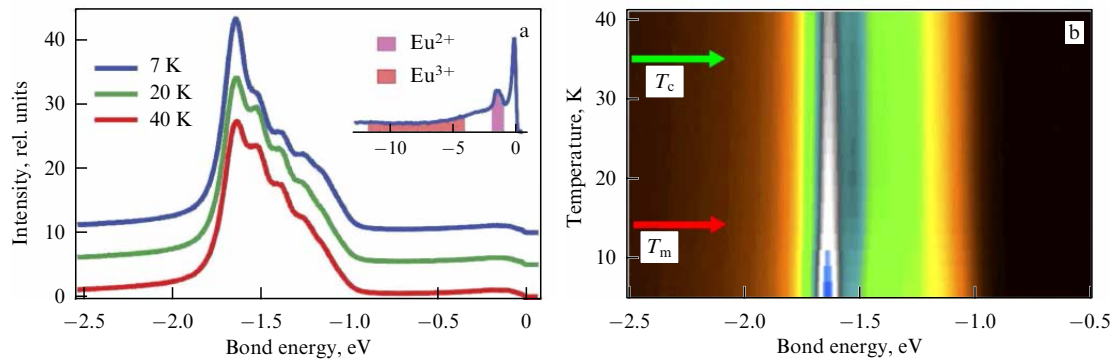

Figure 8. (Color online.) (a) Resonant photoemission spectra of Eu $4d \rightarrow 4f$ measured at temperatures of 7, 20, and 40 K. Off-resonant 120 eV survey scan shown as inset indicates no admixture of the Eu^{3+} state. (b) Two-dimensional color presentation of the intensity evolution of the Eu^{2+} 4f resonant photoemission signal in the temperature range from 40 to 5 K, where white (blue) corresponds to the photoemission intensity maximum, black, to the intensity minimum. Two arrows mark the temperature of magnetic ordering and superconducting transition. (Adapted from [36].)

the valence band spectrum with no spectral structure in the binding energy range of 5–8 eV, which would indicate the presence of trivalent Eu. This clearly proves that the Eu atoms in EuRbFe$_4$As$_4$ are in the Eu^{2+} state, without an admixture

of the Eu^{3+} states. The magnetic moment of Eu $6.97\mu_B$ calculated within the DFT also agrees well with the experiment.

Electronic spectra in Ref. [36] have been calculated within the DFT for three different types of Eu magnetic moment ordering: FM, AFM-180, and AFM-90, matching fully ferromagnetic ordering and helical AFM ordering with the magnetization vector rotating between adjacent Eu layers by an angle of 180° and 90°, respectively. The latter configuration was theoretically suggested in Ref. [25] and reported experimentally from Bragg's neutron scattering [24]. The calculations in Ref. [36] showed that, regardless of the type of magnetic ordering of Eu, the bands forming electronic M-pockets at the Fermi level are almost completely determined by the $d_{xz(yz)}$ orbitals of Fe, whereas the bands forming hole Γ-pockets are determined by a mixture of different Fe 3d orbitals. The main result of these calculations is that the band structure at the Fermi level and the orbital character of Fe 3d bands are almost unaffected by the type of magnetic ordering of Eu 4f magnetic moments. For this reason, the pairing interaction among Fe 3d itinerant electrons is insensitive to the onset of the local magnetic order of Eu atoms.

By comparing the total energies of three different configurations of Eu magnetic ordering, it was found in Ref. [36] that the AFM-90 configuration is energetically most favorable. The total energy of AFM-180 is 1.8 meV/f.u. higher, whereas the FM configuration is the least favorable, being 4.4 meV/f.u. higher in energy than AFM-90 [36].

3. Conclusion

In the last three years, the recently discovered magnetic superconductor of the stoichiometric composition $EuRbFe_4As_4$ has been the focus of intensive experimental research, including high resolution ARPES and ResPES, STS, Andreev spectroscopy, electron spin resonance (ESR), infrared spectroscopy, and measurements of thermodynamic properties. As a result of these comprehensive experimental studies and theoretical *ab initio* DFT calculations, the helicoidal type of magnetic ordering of the Eu moments was confirmed; it was theoretically established that the lowest energy is intrinsic to the helicoidal-type AFM-90 of magnetic structure with magnetization vector rotation by 90° between the Eu layers.

ARPES measurements showed that the band structure of EuRb-1144 is very similar to that of parent compounds of the 122 family of iron-based superconducting non-magnetic pnictides. The band structure measured by ARPES and confirmed by STS is in agreement with the theoretically calculated one. These results clearly show the position of Eu levels with a high spectral density at ~ 1.7 eV below the Fermi energy.

DFT calculations also indicate that the type of magnetic ordering is weakly reflected in the electronic spectrum of the 3d itinerant Fe states near the Fermi level, which participate in the superconducting pairing. Measurements of superconducting properties using thermodynamic techniques, ARPES, and Andreev spectroscopy have identified a fully gapped state with the s-type symmetry of the order parameter, slightly anisotropic in the $k_x - k_y$ plane. Temperature dependences of the order parameter amplitude for different pockets of the FS are consistent with the BCS model. In this way, the superconducting properties of EuRb-1144, in general, turn

out to be almost insensitive to Eu magnetic ordering itself and to its type.

However, one cannot extend the results described here too broadly or assume that superconductivity and magnetic ordering are completely independent. In recent paper [40], it was predicted that the magnetic ordering at $T = T_m$ should affect the density of the superconducting condensate ρ_s rather than the amplitude of the superconducting order parameter. The first measurements of the spatial profile of Abrikosov vortices [41] confirm this theoretical prediction. An anomaly in specific heat at $T = 15$ K found in Ref. [42] was interpreted by the authors as the Berezinskii–Kosterlitz–Thouless (BKT) transition. The temperature evolution of the ESR line was also discussed in terms of the BKT topological transition [43].

Another interesting question is the mechanism for establishing the long-range magnetic order of Eu layers: since the $Eu - Eu$ spacing is too large (1.3 nm), the itinerant electrons of the Fe orbitals simultaneously participate in s-type pairing and transfer the spin moment between the Eu layers. Nor can one rule out the existence of phase transitions between various types of magnetic ordering, including more complex ones than the helix.

References

1. Zapf S, Dressel M *Rep. Prog. Phys.* **80** 016501 (2017)
2. Paglione J, Greene R L *Nat. Phys.* **6** 645 (2010)
3. Si Q, Yu R, Abrahams E *Nat. Rev. Mater.* **1** 16017 (2016)
4. Dutta A et al. *J. Phys. Condens. Matter* **25** 375602 (2013)
5. Cao G et al. *J. Phys. Condens. Matter* **23** 464204 (2011)
6. Ren Z et al. *Phys. Rev. Lett.* **102** 137002 (2009)
7. Nowik I et al. *J. Phys. Condens. Matter* **23** 065701 (2011)
8. Stolyarov V S et al. *Sci. Adv.* **4** aat1061 (2018)
9. Veshchunov I S et al. *JETP Lett.* **105** 98 (2017); *Pis'ma Zh. Eksp. Teor. Fiz.* **105** 87 (2017)
10. Nandi S et al. *Phys. Rev. B* **89** 014512 (2014)
11. Devizorova Zh, Mironov S, Buzdin A *Phys. Rev. Lett.* **122** 117002 (2019)
12. Ghigo G et al. *Phys. Rev. Research* **1** 033110 (2019)
13. Grebenchuk S Yu et al. *Phys. Rev. B* **102** 144501 (2020)
14. Devizorova Zh, Buzdin A *Phys. Rev. B* **100** 104523 (2019)
15. Müller K-H, Narozhnyi V N *Rep. Prog. Phys.* **64** 943 (2001)
16. Iyo A et al. *J. Am. Chem. Soc.* **138** 3410 (2016)
17. Anderson P W, Suhl H *Phys. Rev.* **116** 898 (1959)
18. Vlasko-Vlasov V K et al. *Phys. Rev. B* **99** 134503 (2019)
19. Stolyarov V S et al. *J. Phys. Chem. Lett.* **11** 9393 (2020)
20. Bao J-K et al. *Cryst. Growth Des.* **18** 3517 (2018)
21. Liu Y et al. *Phys. Rev. B* **93** 214503 (2016)
22. Hao J et al. *Chinese Phys. B* **22** 087410 (2013)
23. Liu Y et al. *Sci. Bull.* **61** 1213 (2016)
24. Iida K et al. *Phys. Rev. B* **100** 014506 (2019)
25. Koshelev A E *Phys. Rev. B* **100** 224503 (2019)

26. Vlasenko V, Pervakov K, Gavrilkin S *Supercond. Sci. Technol.* **33** 084009 (2020)
27. Bean C P *Rev. Mod. Phys.* **36** 31 (1964)
28. Kuzmicheva T E et al. *JETP Lett.* **104** 852 (2016); *Pis'ma Zh. Eksp. Teor. Fiz.* **104** 864 (2016)
29. Kuzmicheva T E et al. *Phys. Usp.* **57** 819 (2014); *Usp. Fiz. Nauk* **184** 888 (2014)
30. Kuzmicheva T E et al. *Europhys. Lett.* **102** 67006 (2013)
31. Abdel-Hafiez M et al. *Phys. Rev. B* **97** 134508 (2018)
32. Bezotosnyi P I et al. *Phys. Rev B* **100** 184514 (2019)
33. Majumdar A et al. *Phys. Rev. Mater.* **4** 084005 (2020)
34. Kümmel R, Gunsenheimer U, Nicolsky R *Phys. Rev. B* **42** 3992 (1990)
35. Moreland J, Ekin J W *J. Appl. Phys.* **58** 3888 (1985)
36. Kim T K et al. *Phys. Rev. B* **103** 174517 (2021)
37. Evtushinsky D V et al. *Phys. Rev. B* **79** 054517 (2009)
38. Evtushinsky D V et al. *Phys. Rev. B* **89** 064514 (2014)
39. Ding H et al. *Europhys. Lett.* **83** 47001 (2008)
40. Koshelev A E *Phys. Rev. B* **102** 054505 (2020)
41. Collomb D et al. *Phys. Rev. Lett.* **126** 157001 (2021)
42. Willa K et al. *Phys. Rev. B* **99** 180502 (2019)
43. Hemmida M et al. *Phys. Rev. B* **103** 195112 (2021)